Gaussian Process Based Model to Optimize Additively Manufactured Powder Microstructures from Phase Field Modeling

Arunabha Batabyal[1], Sugrim Sagar, Jian Zhang, Tejesh Dube, Xuehui Yang, Jing Zhang*

Department of Mechanical and Energy Engineering

Indiana University-Purdue University Indianapolis, Indianapolis, IN 46022, USA

*Corresponding author: jz29@iupui.edu

Abstract

A persistent problem in the selective laser sintering process is to maintain the quality of additively manufactured parts, which can be attributed to the various sources of uncertainty. In this work, a two-particle phase-field microstructure model has been analyzed using Gaussian Process based model. The sources of uncertainty as the two input parameters were surface diffusivity and inter-particle distance. The response quantity of interest (QOI) was selected as the size of the neck region that develops between the two particles. Two different cases with equal and unequal-sized particles were studied. It was observed that the neck size increased with increasing surface diffusivity and decreased with increasing inter-particle distance irrespective of particle size. Sensitivity analysis found that the inter-particle distance has more influence on variation in neck size than that of surface diffusivity. The machine learning algorithm Gaussian Process Regression was used to create the surrogate model of the QOI. Bayesian Optimization method was used to find optimal values of the input parameters. For

[1] Present address: Department of Industrial and Systems Engineering, The University of Iowa, Iowa City, IA 52242, USA

This is the author's manuscript of the article published in final edited form as:

Batabyal, A., Sagar, S., Zhang, J., Dube, T., Yang, X., & Zhang, J. (2021). Gaussian Process-Based Model to Optimize Additively Manufactured Powder Microstructures From Phase Field Modeling. ASCE-ASME J Risk and Uncert in Engrg Sys Part B Mech Engrg, 8(1). https://doi.org/10.1115/1.4051745

equal-sized particles, optimization using Probability of Improvement provided optimal values of surface diffusivity and inter-particle distance as 23.8268 and 40.0001, respectively. The Expected Improvement as an acquisition function gave optimal values 23.9874 and 40.7428, respectively. For unequal-sized particles, optimal design values from Probability of Improvement were 23.9700 and 33.3005, respectively, while those from Expected Improvement were 23.9893 and 33.9627, respectively. The optimization results from the two different acquisition functions seemed to be in good agreement.

Keywords: Powder; Microstructure; Additive manufacturing; Machine learning; Optimization

1. Introduction

Selective laser sintering (SLS) is an additive manufacturing technique that uses a laser as the power source to sinter powdered material, aiming the laser automatically at points in space defined by a 3D model, binding the material together to create a solid structure [1, 2]. This process has been widely used in aerospace and automotive sectors for preparing complex parts with unconventional geometries which were not possible previously by conventional subtractive manufacturing techniques. The sintering kinetics is characterized by multiple diffusion paths, particle rigid-body motion, and grain-growth through boundary migration [3]. Sintering can also be used as heat treatment in order to increase the strength and integrity of a material. This material processing technique is very useful for custom shaping materials that have high melting points. Materials can be produced with uniform porosity and preserved purity. Efficient control of evolving morphologies like inter-particle neck region and grain boundary is necessary for better mechanical and thermal properties and an optimized manufacturing process.

In the current work, microstructure evolution has been studied during the selective laser sintering process. During the process, morphologies such as densification and grain growth occur. The proper control of these structural evolutions is necessary for better mechanical properties of the material. Sintering takes place due to the diffusion of atoms through the microstructure of the material. The diffusion results due to a gradient in chemical potential i.e., atoms move from a region of higher chemical potential to that of a lower chemical potential. Diffusion takes place by several mechanisms like surface diffusion, vapor transport, lattice diffusion from the surface, lattice diffusion from grain boundary, grain boundary diffusion, plastic diffusion, etc. Higher densification is preferred to reduce porosity in the material and smaller grain growth is desired. The microstructure evolution is driven by a reduction of total system free energy through diffusion and structural relaxation[3]. The particle rigid-body

motion that occurs during sintering is driven by the diffusion of atoms from grain boundaries to nearby growing neck surface and thus leads to the formation of neck region between two particles. In Ref. [4], it is found that enhancing both neck size and neck growth rate and may lead to the formation of dense samples with further increases in processing time or temperature. In Ref. [5], the in situ strength during sintering was determined by the competition among interparticle neck growth, densification, and thermal softening.

Analysis of the simulation models has found an expression for the rate of change of neck size ratio as a function of sintering time [6]:

$$\left(\frac{X}{D}\right)^{n} = Kt \quad (1)$$

where X refers to the neck width and D the diameter of the particle. K is related to material properties and geometric assumptions. Due to the growing neck size between the particles, sintering provides strength which can be formulated as [6, 7]:

$$\sigma_B = \sum_{1}^{N_c} V_s \frac{N_c}{\pi}\left(\frac{X}{D}\right)^{2} \quad (2)$$

where σ_B is the bulk sintering strength, summing about the packing coordination N_c, $\sum$ is the summation sign, V_s is solid volumetric fractional density, and $\frac{X}{D}$ is the neck size to particle size ratio.

However, one persistent concern in this material processing methodology as in other manufacturing technologies has been to produce parts with desired properties. Even if the same parameters are used during the manufacturing process of a specific product, it is not possible to acquire uniform properties. Pavan *et al.* used X-ray Computed Tomography (CT) based approach to study the effect of features' size and printing orientation on the porosity and shape

deviation of each feature in laser sintering for polymers processing [8]. Several replicas of the test object were made for polyamide-12 to analyze the reproducibility of the manufacturing process. It was observed that porosity levels of small features depend on their size and orientation with a smooth increase in voids' content with increased size. Also features oriented along printing direction showed an overall higher porosity value with bigger average pore sizes independent of the size of the feature. Dotchev *et al.* investigated polyamide 12 (PA12) powder properties deterioration in the laser sintering process by artificially aging new and recycled grades of PA2200 powder in a temperature-controlled oven and tested using melt flow rate (MFR) indexer [9]. It was found that the powder exposed at a higher temperature and longer time experienced a higher deterioration rate. Also, powder located at the periphery and top of the build is less deteriorated than that at the center or the bottom of a long build. Karapatis *et al.* tried to find out to what extent the density of thin powder layers can be increased for controlling the quality of selective laser sintered parts [10]. Experiments showed that the density of thin layers increased from 53% to 63% when 30% fine powder was added to a coarse powder with a coarse-to-fine ratio of 1:10. However, this density improvement method was found to be less efficient as the particle do not arrange as efficiently. Zarringhalam *et al.* showed that differential scanning calorimetry (DSC) has a good potential for quality control of selective laser-sintered parts [11]. DSC analysis of SLS Nylon-12 parts showed the presence of two distinct melt peaks which correspond to the melted and un-melted regions of the part. Also, it was proved that the amount of energy input during the process affects the degree of melting. Phillips *et al.* provided an approach of controlling temperature non-uniformity in the Selective Laser Sintering (SLS) process through a feed-forward control system [12]. It was evident that a 45% improvement in ultimate flexural strength standard deviation was achieved. Wegner *et al.* integrated a thermal imaging system in a laser sintering machine for process monitoring [13]. Results found that thermal imaging is well-suited for checking on powder bed

surface temperature distribution and the melt's temperature. Olakanmi *et al.* investigated the effect of mixing time on SLS processed density and microstructure [14]. The optimal mixing time was found to be ten minutes above which the density of sintered parts decreased and hence porosity increased. This led to the deterioration of the microstructure of the SLS sintered parts. Olakanmi *et al.* showed that microstructural evolution in laser sintered Al-12Si powder was controlled by specific laser energy input [15].

In addition to experiments, numerical models, such as the phase-field method have been used as an effective tool for modeling co-evolution of microstructure and physical properties at the mesoscale. The microstructure is explained by a system of continuous variables with the interfaces having a finite width over which the variables have varying values. The evolution of the microstructural morphology is described in terms of the free energy of the system. Biswas *et al.* studied the consolidation kinetics during the sintering process using a phase-field modeling approach [16]. It was observed that the initial interactions among particles were due to surface diffusion and then densification was governed by volume and grain boundary diffusion. The grain size kept increasing under pressure and stabilized later when adjacent grains touched each other. Hotzer *et al.* used a phase-field model based on the grand potential approach to study the microstructural evolution during the solid-state sintering process [17]. The neck growth rates and particle approach in a two-particle system were compared with analytic solutions for different diffusion mechanisms and a good agreement was found between the two. Densification results for a three-dimensional green body of 24897 Al_2O_3-grains matched well with the analytic Coble model. Biswas *et al.* investigated the microstructural changes during solid-state sintering using a phase-field model that included rigid-body motion, elastic deformation, and heat conduction [18]. The simulations showed three distinctive stages during the sintering process - neck and grain boundary formation, neck length growth and stabilization, rapid grain growth, and disappearance of one of the grains. Morphology evolution

was found to be contributed by the radius of particles, the curvature at neck location, surface energy, grain boundary energy, and variation in temperature. Asp *et al.* presented a phase-field model of sintering and related phenomena in a two-phase system and multi-phase system using diffusion of vacancies as the mechanism for redistribution of material [19]. The solid body was characterized by a low vacancy content, the surroundings by a high vacancy content, and the surface with varying vacancy content. The temporal development of particles during solid-state sintering with wetting effects was shown in the simulations. Kumar *et al.* modeled sintering and simultaneous concurrent grain growth of two unequal-sized particles using a phase-field method [20] The simulation revealed to have three sub-processes: neck growth, coarsening with concurrent slow grain boundary migration, and rapid grain boundary motion. The simulation results were analyzed based on thermodynamic analysis of the driving forces for different sub-processes. The slow grain boundary migration was found to be sensitive to sintering geometry. Dzepina *et al.* incorporated the contact mechanics algorithm into a phase-field sintering model [21]. Energy relaxation maintained contact between the particles through deformation was achieved by diffusive fluxes along stress gradients and rigid body motion of the deforming particles. The effect of applied pressure on high pressure-high temperature (HPHT) liquid phase sintering of diamond particles was investigated and changes in neck size, particle coordination, and contact flattening were observed. Termuhlen *et al.* introduced an approach for incorporating individual particle rigid-body motion during three-dimensional phase-field sintering simulation [22]. A grouping algorithm was introduced with a cut-off radius set on each grain to calculate the particle velocity during densification. This allowed for the incorporation of densification mechanisms into the three-dimensional phase-field sintering model.

Recently machine learning and artificial intelligence (AI) have been used to study the sintering phenomena. Swaroop *et al.* proposed a machine-learning based approach to predict abnormal

grain growth in powdered samples before actual sintering [23]. The approach was found to have the potential to allow for the pre-selection of appropriate powder samples with an accuracy of 82%. This way of controlling abnormal grain growth could help reduce porosity and hence the enhancement of sintered material properties. Song *et al.* proposed a comprehensive prediction model of sinter quality based on a machine learning approach [24]. Classification model of sinter quality and regression model of sinter's total iron content was established using different machine learning algorithms. Results showed that the prediction accuracy of the classification model and regression model inferred by the extra tree is the best. The F1-score of the quality index classification model was found to be 0.92 and R^2 of the total iron content regression model was 0.882 thus indicating good learning and generalization ability of the proposed framework. Xiao *et al.* applied a deep convolution neural network to detect three typical types of powder bed defects in the selective laser sintering process: warpage, part shifting, and short feed [25]. The method was found to have good accuracy and efficiency and was able to cope with geometrical distortion and image blurring. Wu *et al.* established a method for rapid evaluation of the effect of heating rate on sintering densification based on the domain-adversarial neural network [26]. This allowed for the prediction of densification evolution of a material that lacked a master sintering curve (MSC) from MSC data of another material. The proposed approach could provide an efficient solution to the issue of data scarcity in the sintering field. Zhang *et al.* presented a multi-objective optimization and analysis model of the sintering process based on the BP neural network [27]. Genetic algorithms combined with BP neural network reduced the learning time and increased the forecasting accuracy of the network model. The relation between factors like quality and multi-objective was analyzed with the results being consistent with the process.

The extensive experimental and modeling efforts produced some good results, however, one persistent concern in high-demand manufacturing technology has been to produce parts with

controlled desirable properties. Even if the same parameters are used during the manufacturing process of a specific product, it is not possible to acquire uniform properties. For modeling approaches to study the different phases of the additive manufacturing technique, a little variation in any of the models will contribute to the final uncertainty of the prediction of the quality of the manufactured part.

Therefore, the motivation of this work is that since neck size is directly related to the quality and strength of the sintered part, there is a need to develop a methodology to optimize the neck size. The objective is to use a machine learning approach to find out optimal values of surface diffusivity and inter-particle distance for maximizing neck size for equal and unequal sized particles and quantify the uncertainty. The structure of the current paper is as follows. Section 2 elaborates the model details and mechanisms i.e., the phase-field model for simulation of neck growth in a two-particle system, surrogate models via Machine Learning approach, sensitivity analysis, and surrogate-based input parameter optimization through a Bayesian Optimization algorithm. Section 3 lists all the results and discussion. Section 4 concludes the paper with major points.

2. Numerical model details

2.1 Phase-field model of powder sintering

2.1.1 Governing equations of the phase-field microstructural model

In the present study, the phase-field model and its codes for sintering in Ref. [28] have been adopted for the current work to generate the microstructures of the two-particle model. The values used in this work are based on Ref. [3]. As stated in Ref. [3], the equations are also nondimensionalized with respect to the computational grid size and the energy barrier between the two coexisting phases. These parameters give a diffusivity ratio of about 1000:100:10:1 along surface and grain boundary, through volume and vapor, respectively,

and an interfacial energy density ratio of about 2:1 between surface and grain boundary. These values could also be taken from physical quantities related to specific materials. The microstructure is defined by the free energy function of the system which is mathematically represented as:

$$F = \int_v [f(\rho, \eta 1, \ldots p) + \frac{k_\rho}{2}(\nabla\rho)^2 + \sum_i \frac{k_\eta}{2}(\nabla\eta_i)^2]dv \quad (3)$$

where $k_\rho$and k_η are gradient energy coefficients for concentration and grain boundary energies respectively [28]. The evolution equation for the density field follows the Cahn-Hilliard equation:

$$\frac{\partial\rho}{\partial t} = \nabla.\left(\frac{D\nabla\delta\mathrm{F}}{\delta\rho}\right) = \nabla.\,\mathrm{D}\nabla\left(\frac{\partial\mathrm{f}}{\partial\rho} - k_\rho\nabla^2\rho\right) \quad (4)$$

where D is the microstructure-dependent diffusivity coefficient [28]. D is assumed to take the form:

$$D = D_{vol}\phi(\rho) + D_{vap}[1-\phi(\rho)] + D_{surf}\rho(1-\rho) + D_{GB}\sum_i\sum_{i\neq m}\eta_i\eta_m \quad (5)$$

where D_{vol} is the bulk diffusivity, D_{vap} is the diffusivity of the vapor phase, D_{surf} is the surface diffusivity and $D_{GB}$is the grain boundary diffusivity.

The non-conserved order parameter which represents the particles and the grain boundaries follows the Allen-Cahn equation:

$$\frac{\partial\eta_i}{\partial t} = -\frac{L}{\partial\eta_i}\delta F = -L\left(\frac{\partial F}{\partial\eta_i} - k_\eta\nabla^2\eta_i\right) \quad (6)$$

where L is grain-boundary mobility [28].

The Cahn-Hilliard and Allen-Cahn governing equations were solved with a finite-difference algorithm by using the five-point stencil in two-dimensional space. The time integration was carried out by a simple explicit Euler time marching scheme.

2.1.2 Geometry and mesh of equal size and unequal size two-particle models

For equal-sized particles, the radii of the two spherical particles were made equal and the model was simulated for 20,000 time steps. The radius of each particle was 20 units. The simulation cell was discretized into 100 grid points in the x-direction and 100 grid points in the y-direction. The grid spacing was 0.5 in both x and y directions. The inter-particle distance was kept as 40 units initially and was varied according to the uniform distribution.

For unequal-sized particles, the radius of one of the spherical particles was made 1.5 times that of the other and the phase-field model was simulated for 20,000 time steps. The radius of one particle was 20 and that of the other was 40/3. The simulation cell was discretized into 100 grid points in the x-direction and 100 grid points in the y-direction. The grid spacing was 0.5 in both x and y-directions. The inter-particle distance varied from 33.3 through 34.8.

2.1.3 Material properties

The gradient coefficient for the concentration field k_ρ was set to 5.0, the gradient coefficient for order parameters k_η was assigned value of 2.0, mobility of order parameters L set as 10.0 [28]. The value of bulk diffusivity D_{vol} was 0.04, diffusivity of the vapor phase D_{vap} 0.002, initial surface diffusivity D_{surf} 16.0, grain boundary diffusivity D_{GB} 1.6 [28]. Since the values in the phase-field model were normalized, the temperature was not considered as an explicit

input parameter. However, the temperature effect can be included by using temperature-dependent material properties.

2.1.4 Boundary conditions

The concentration field which takes the value of 1 in the particles and 0 elsewhere was initialized to 0. It is a one-dimensional array and can be represented as $con(N_x N_y)$. The two-dimensional array of non-conserved order parameters for the particles $etas(N_x N_y, npart)$ was initialized to 0. $N_x N_y$ represents the total number of grid points in the simulation cell and $npart$ is the number of particles.

2.2 Machine learning approach

2.2.1 Gaussian process regression

A Gaussian Process is a set of random variables, any finite number of which have joint Gaussian distributions [29]. A random variable is any variable whose value depends on the outcome of a random phenomenon. Any random variable can be described by its cumulative distribution function which describes the probability (P) that the random variable will be less than or equal to a certain value. The cumulative distribution function can be described as:

$$F_X(x) = P(X \leq x) \quad (7)$$

where X is the random variable and x is the target value. A joint distribution is used when we want to study two random variables together. For instance, the joint cumulative distribution function of two random variables X and Y can be represented as:

$$F_{XY}(x, y) = P(X \leq x, Y \leq y) \quad (8)$$

which can also be represented as:

$$F_{XY}(x, y) = P((X \leq x) \text{ and } (Y \leq y)) = P((X \leq x) \cap (Y \leq y)) \quad (9)$$

A Gaussian Process consists of a mean function *m(x)* and a covariance function *k(x, x')*. The Gaussian distribution can be indicated as:

$$f \sim GP(m, k) \quad (10)$$

which means the function *f* is distributed as a Gaussian Process with mean function *m* and covariance function *k* [29]. The individual random variables in a vector from a Gaussian distribution are indexed by their position in the vector. For example, if the input variable is denoted by *x*, then for each input *x*, there is an associated random variable *f(x)* which is the value of the stochastic function *f* at that location. The Gaussian process prediction, known as Kriging, has a basis function that can be formulated as [30]:

$$\psi^i = \exp\ (-\sum_{j=1}^{k} \theta_j \left| x_j^{(i)} - x_j \right|^{p_j}) \quad (11)$$

The θ in the equation above allows the width of the basis function to vary from variable to variable [30]. The varying value of p_j allows for the smoothness to vary for the function. As mentioned earlier, each input variable has an associated random output variable, so the observed responses can be denoted by a set of random vectors:

$$\boldsymbol{Y} = \begin{pmatrix} Y(x^1) \\ \vdots \\ Y(x^n) \end{pmatrix} \quad (12)$$

The random vector has a mean of $\mathbf{1}\mu$ where $\mathbf{1}$ is an $n \times 1$ column vector of ones, and n represents the number of observations. The random variables are correlated with each other by the expression:

$$cor\left[Y\left(x^i\right), Y(x^l)\right] = \exp\left(-\sum_{j=1}^{k} \theta_j \left|x_j^i - x_j^l\right|^{p_j}\right) \qquad (13)$$

From Eq. 13, an $n \times n$ correlation matrix can be constructed for the observed samples:

$$\boldsymbol{\Psi} = \begin{pmatrix} cor[Y(x^1), Y(x^2)] & \cdots & cor[Y(x^1), Y(x^n)] \\ \vdots & \ddots & \vdots \\ cor[Y(x^n), Y(x^1)] & \cdots & cor[(Y(x^n), Y(x^n)] \end{pmatrix} \qquad (14)$$

A covariance matrix can be created from the above correlation matrix [30]:

$$Cov(\boldsymbol{Y}, \boldsymbol{Y}) = \sigma^2 \boldsymbol{\Psi} \qquad (15)$$

Correlation refers to the degree to which two random variables are linearly related to each other. There are several correlation coefficients like the Pearson correlation coefficient, Spearman's rank correlation coefficient, Kendall's rank correlation coefficient, etc. The value of the correlation coefficient can vary between -1 and +1. A value of +1 refers to a perfect linearly increasing relationship between the two variables. A value of -1 refers to a perfect linearly decreasing relationship between the variables. A value of 0 refers to no correlation or dependence between the variables. The closer the coefficient is to -1 or +1, the stronger the correlation is between the variables. Covariance is defined as the correlation between two or more sets of random variables. For two random variables X and Y ,

$$Cov(X, Y) = E\left[(X - \mu_x)\left(Y - \mu_y\right)\right] = E[XY] - \mu_x \mu_y \qquad (16)$$

where μ_x and μ_y are the means of X and Y and E is the expectation. The relation between correlation and covariance can be represented as [30]:

$$cor(X,Y) = \frac{cov(X,Y)}{\sigma_x \sigma_y} \qquad (17)$$

The correlation between the elements of $\boldsymbol{Y}$ depends on the values of absolute distance between the sample points $\left|x_j^i - x_j^l\right|$, the parameters p_j and θ_j. It has been observed that as the two points move close together i.e., $x_j^i - x_j^l \to 0$, $\exp\left(-\left|\mathrm{x_j^i} - \mathrm{x_j^l}\right|^{\mathrm{p_j}}\right) \to 1$ i.e., the points show highly increasing linear correlation whereas when the distance$\to \infty$, the correlation coefficient$\to 0$, i.e., the points do not correlate. θ_j is a width parameter that affects how far a data point's influence extends. A low θ_j means all data points have a high correlation [30] while the reverse is true for a high θ_j. Hence θ_j can be considered as a measure of how active the approximating function is. The value of θ and p can be found out by maximizing the likelihood of the observed responses $\boldsymbol{Y}$. Taking the natural logarithm of likelihood :

$$\ln(L) = -\frac{n}{2}\ln(2\pi) - \frac{n}{2}\ln(\sigma^2) - \frac{1}{2}\ln|\boldsymbol{\Psi}| - \frac{(\boldsymbol{y} - \boldsymbol{1}\mu)^T \boldsymbol{\Psi}^{-1} (\boldsymbol{y} - \boldsymbol{1}\mu)}{2\sigma^2} \qquad (18)$$

The maximum likelihood estimates (MLEs) for μ and σ^2:

$$\hat{\mu} = \frac{\boldsymbol{1}^T \boldsymbol{\Psi}^{-1} \boldsymbol{y}}{\boldsymbol{1}^T \boldsymbol{\Psi}^{-1} \boldsymbol{1}} \qquad (19)$$

$$\hat{\sigma}^2 = \frac{(\boldsymbol{y} - \boldsymbol{1}\mu)^T \boldsymbol{\Psi}^{-1} (\boldsymbol{y} - \boldsymbol{1}\mu)}{n} \qquad (20)$$

The concentrated ln-likelihood function can be denoted as [30]:

$$\ln(L) \approx -\frac{n}{2}\ln(\sigma^2) - \frac{1}{2}\ln|\boldsymbol{\Psi}| \qquad (21)$$

The values of $\theta \; and \; p$ are found to maximize the above ln-likelihood function. This is usually done through a genetic algorithm or exhaustive search function. The maximum likelihood estimate (MLE) for the Kriging prediction $\hat{y}$ is given by [30]:

$$\hat{y}(\boldsymbol{x}) = \hat{\mu} + \boldsymbol{\psi}^T \boldsymbol{\Psi}^{-1}(\boldsymbol{y} - \mathbf{1}\hat{\mu}) \quad (22)$$

2.2.2 Surrogate modeling

Surrogate models are approximations of the original simulation model. In this work, the Gaussian Process Regression (Kriging) methodology has been used here to build the surrogate models that predict neck size from input parameters surface diffusivity and inter-particle distance. A 4-level full factorial Design of Experiments (DOE) was performed in the process of creating the surrogate model. First, the design variables and response variables were determined. In this case, the design variables were surface diffusivity and the inter-particle distance. The response variable was certainly the size of the evolved neck region in-between the two spherical particles. The statistical design of experiments allows varying variables simultaneously rather than varying one-factor-at-a-time [31]. This way the mutual interactions between the variables are also considered. So the quantity of interest neck size can be modeled as a function of these two design variables:

$$N = f\left(D_{surf}, d\right) \quad (23)$$

where N refers to the neck size, D_{surf} stands for surface diffusivity and d refers to the inter-particle distance.

2.2.2.1 Training data

Table 1 and Table 2 show the DOE matrix for equal-sized and unequal-sized particles respectively. Sixteen simulations of the phase-field model were performed at varying values of

the input parameters. A uniform distribution of data was considered for both surface diffusivity and inter-particle distance. For equal-sized particles, the range of surface diffusivity was [4, 24] and that for inter-particle distance [40, 41.5] while for unequal-sized particles, the ranges were [4, 24] and [33.3, 34.8] respectively. There was not much difference in values of neck size at higher time steps. Hence, in order to reduce computational expense, the total time steps were kept at 5000, and the neck size after each simulation was noted. The trend in response values was found to be monotonic, so even if more simulations were performed, the additional data points would be on the same surfaces.

Table 1: DOE matrix for equal-sized particles model

Serial No.	Surface diffusivity (D_{surf})	Inter-particle distance (d)	Neck size(N)
1	4	40	14.15388
2	8	40	15.50387
3	16	40	17.18751
4	24	40	19.36508
5	4	40.5	12.40309
6	8	40.5	13.95348
7	16	40.5	15.748
8	24	40.5	16.69287
9	4	41	8.00002
10	8	41	9.53848
11	16	41	12.1875

12	24	41	14.1732
13	4	41.5	5.84617
14	8	41.5	7.75193
15	16	41.5	10.39367
16	24	41.5	12.28342

Table 2: DOE matrix for unequal sized particles model

Serial No.	Surface diffusivity (D_{surf})	Inter-particle distance (d)	Neck size (N)
1	4	33.3	12.093
2	8	33.3	13.2308
3	16	33.3	14.68752
4	24	33.3	15.55554
5	4	33.8	10.46155
6	8	33.8	11.47285
7	16	33.8	13.22831
8	24	33.8	14.28572
9	4	34.3	6.82169
10	8	34.3	8.37208
11	16	34.3	10.39367

12	24	34.3	12.06348
13	4	34.8	4.30771
14	8	34.8	6.76924
15	16	34.8	9.06252
16	24	34.8	10.39367

Observations 4, 5, 6, and 7 in both Table 1 and Table 2 were kept aside for the model testing purpose and were not used for generating the metamodels.

2.2.2.2 Metamodel generation

The metamodel was generated from the training data through Gaussian Process Regression. The ooDACE toolbox was used for the creation of the surrogate model [32]. A fourth of the data in Tables 1 and 2 were left out and kept reserved for testing the accuracy of the model. The lower bound and upper bound of the hyper-parameters were fixed at [-5 5]. Three Gaussian regression functions of orders zero, one, and two were tested for building the metamodel. A mesh grid of size 100×100 was created to plot the surface of neck size.

2.2.2.3 Model testing

For model testing purposes, the root mean squared error (RMSE) can be used as a metric [30]. If the available observed data is enough, $0.25n$ $x \rightarrow y$ pairs can reserved for model testing [33]. RMSE can be formulated as:

$$\sqrt{\frac{\sum_{i=0}^{n_t}(y^i - \hat{y}^i)^2}{n_t}} \qquad (24)$$

where n_t is the number of observations for testing, y^i is the i^{th} observation and $\hat{y}^i$ is the prediction corresponding to the i^{th}observation [30].

Table 3: Model testing data for equal-sized particles

Serial No.	Surface diffusivity (D_{surf})	Inter-particle distance (d)	Neck size(N)
1	24	40	19.36508
2	4	40.5	12.40309
3	8	40.5	13.95348
4	16	40.5	15.748

Table 4: Model testing data for unequal sized particles

Serial No.	Surface diffusivity (D_{surf})	Inter-particle distance (d)	Neck size(N)
1	24	33.3	15.55554
2	4	33.8	10.46155
3	8	33.8	11.47285
4	16	33.8	13.22831

2.2.2.4 Cross-validation

Cross-validation is a technique to test how accurately a predictive model will perform in real life. The goal is to test the model's ability to predict new data that was not used as training data. This can help to avoid problems like overfitting or underfitting of the model and generalize the model for working on unknown datasets. Cross-validation involves partitioning the data into subsets called training set and validation set. In one round, the model is built using the training set and validated using the validation/testing set. Multiple rounds are performed like this with different subsets to reduce variability. The prediction error is found in each round. The average error for all rounds gives an estimate of the accuracy of the predictive capability of the model. There are two types of cross-validation methods: Exhaustive and Non-exhaustive. The exhaustive methods include Leave-p-out cross-validation, Leave-one-out cross-validation, while the non-exhaustive methods include k-fold cross-validation, the Holdout method, Repeated random sub-sampling validation. In this work, the Leave-one-out cross-validation (LOOCV) has been used to evaluate the surrogate model. In LOOCV, the dataset is divided into k subsets where k equals the total number of observations. The function approximator is trained on all the data except for one point and prediction is made for that point. The average error is computed from all such predictions. Though it can be a little computationally expensive, it gives an accurate measure of the predictability of the machine-learning model. The advantage is that the variance is reduced to a minimum and it does not depend on how the dataset is subdivided, unlike other cross-validation methods. Mathematically, if a mapping $\zeta: \{1, \dots, n\} \to \{1, \dots, k$ describes the allocation of n training points to one of the k subsets and $\hat{f}^{-i}$ is the value of the predictor obtained by removing the subset $\zeta(i)$, the cross-validation measure can be depicted as [30]:

$$\epsilon_{CV} = \frac{1}{n}\sum_{i=1}^{n} |y^i - \hat{f}^{-i}| \qquad (25)$$

where the absolute error has been taken into account between the i^{th} test response and the i^{th} predicted value.

Table 5: Cross-validation data for equal-sized particles model

Serial No.	Surface diffusivity (D_{surf})	Inter-particle distance (d)	Neck size(N)
1	4	40	14.15388
2	8	40	15.50387
3	16	40	17.18751
4	24	40	19.36508
5	4	40.5	12.40309
6	8	40.5	13.95348
7	16	40.5	15.748
8	24	40.5	16.69287
9	4	41	8.00002
10	8	41	9.53848
11	16	41	12.1875
12	24	41	14.1732
13	4	41.5	5.84617
14	8	41.5	7.75193
15	16	41.5	10.39367
16	24	41.5	12.28342

Table 6: Cross-Validation data for unequal sized particles model

Serial No.	Surface diffusivity (D_{surf})	Inter-particle distance (d)	Neck size (N)
1	4	33.3	12.093
2	8	33.3	13.2308
3	16	33.3	14.68752
4	24	33.3	15.55554
5	4	33.8	10.46155
6	8	33.8	11.47285
7	16	33.8	13.22831
8	24	33.8	14.28572
9	4	34.3	6.82169
10	8	34.3	8.37208
11	16	34.3	10.39367
12	24	34.3	12.06348
13	4	34.8	4.30771
14	8	34.8	6.76924
15	16	34.8	9.06252

16	24	34.8	10.39367

Each observation here was considered a subset. So for each iteration, fifteen sets of training data were available and one set of test (validation) data was present. The error was found in each iteration by subtracting the predicted response from the test response.

2.2.3 Sensitivity analysis

Sensitivity analysis can determine how robust the result is. It can help save time and make informed decisions or choices. Sensitivity Analysis finds out which input variable has more contribution towards the variation of the output response variable. Global Sensitivity Analysis (GSA) takes into account all input variables in a model and determines sensitivity by evaluating the entire range of each input variable [34].

2.2.3.1 Pearson product-moment correlation coefficient

The Pearson product-moment correlation coefficient can be used to determine the contribution of each input parameter on the variability of the response QOI i.e., neck size [35].

$$\text{Corr}\left(D_{surf}, N\right) = \rho_{D_{surf}N} = \frac{\text{Covariance}(D_{surf}, N)}{\sigma_{D_{surf}}\sigma_N} \qquad (26)$$

$$\text{Corr}(d, N) = \rho_{dN} = \frac{\text{Covariance}(d, N)}{\sigma_d \sigma_N} \qquad (27)$$

where D_{surf} is the surface diffusivity, d is the inter-particle distance, N the neck size, $\sigma_{D_{surf}}$, σ_d and σ_N are the standard deviations of D_{surf}, d and N respectively.

2.2.4 Input parameter optimization

2.2.4.1 Bayesian optimization

Bayesian optimization is a class of machine-learning-based optimization methods focused on solving the problem:

$$\underset{x\epsilon A}{\text{Maximize}}\, f(x) \qquad (28)$$

where $f(x)$ is the objective function, x is the input, A is the feasible set. The input x is in $\mathbb{R}^d$ for a value of d that is not too large, typically $d \leq 20$. The feasible set A is a hyper-rectangle $\{x\epsilon\mathbb{R}^d : a_i \leq x_i \leq b_i\}$ or the d-dimensional simplex $\{x\epsilon\mathbb{R}^d : \sum_i x_i = 1\}(2)$. The objective function f is continuous and modeled using Gaussian Process Regression. f usually lacks any known special structure like concavity or linearity that would make it easy to optimize using techniques that leverage such structure to improve efficiency. So f is considered as a black-box. This type of optimization is also referred to as derivative-free optimization as there is no evaluation of first or second-order derivatives. Bayesian optimization consists of two main components: a Bayesian statistical model for modeling the objective function and an acquisition function to decide where to sample next. The statistical model which is usually a Gaussian process provides a Bayesian posterior probability distribution that describes potential values for $f(x)$ at a candidate point x. For each evaluation of f at a new point, the posterior distribution is updated. The acquisition function measures the value that would be generated by evaluation of the objective function at a new infill point x based on current posterior distribution over f. The Gaussian Process-based models permit the calculation of an estimated error in the model, hence it is possible to use this to position infill points where the uncertainty in the prediction of the model is highest. The mean squared error (MSE) in a Gaussian process-based prediction model is [30]

$$\hat{s}^2(\mathbf{x}) = \sigma^2 \left[1 - \boldsymbol{\psi}^T \boldsymbol{\Psi}^{-1} \boldsymbol{\psi} + \frac{1 - \mathbf{1}^T \boldsymbol{\Psi}^{-1} \boldsymbol{\psi}}{\mathbf{1}^T \boldsymbol{\Psi}^{-1} \mathbf{1}}\right] \qquad (29)$$

Using this estimated error, the uncertainty in prediction can be modeled by considering it as the realization of a normally distributed random variable $Y(\mathbf{x})$ with mean $\hat{y}(\mathbf{x})$ and variance $\hat{s}^2(\mathbf{x})$. Considering the possibility that $Y(\mathbf{x})$ can take different values, due to the size of $\hat{s}^2(\mathbf{x})$, infill criteria can be made which balances the values of $\hat{y}(\mathbf{x})$ and $\hat{s}^2(\mathbf{x})$. One way to balance these two is minimizing a statistical lower bound [30]:

$$\mathrm{LB}(\mathbf{x}) = \hat{y}(\mathbf{x}) - A\hat{s}(\mathbf{x}) \qquad (30)$$

where A is a constant that controls the exploitation/exploration balance. As $A \to 0$, $\mathrm{LB}(\mathbf{x}) \to \hat{y}(\mathbf{x})$ (pure exploitation) and as $A \to \infty$, the effect of $\hat{y}(\mathbf{x})$ becomes negligible and minimizing $\mathrm{LB}(\mathbf{x})$ is equivalent to maximizing $\hat{s}(\mathbf{x})$ (pure exploration) [30].

2.2.4.2 Optimization using Probability of Improvement

Usually, the infill point is placed at a value of $\mathbf{x}$ that will help in an improvement on the best observed value so far, i.e., $y_{\min}$ [30]. By considering $\hat{y}(\mathbf{x})$ as the realization of a random variable, the probability of improvement can be calculated as $I = \frac{y_{\min} - Y(\mathbf{x})}{y_{\min}}$ [30].

$$P[I(\mathbf{x})] = \frac{1}{\hat{s}\sqrt{2\pi}} \int_{-\infty}^{0} e^{-[I - \hat{y}(\mathbf{x})]^2/(2s^2)} \mathrm{d}I \qquad (31)$$

Using the error function,

$$P[I(\mathbf{x})] = \frac{1}{2}\left[1 + \mathrm{erf}\left(\frac{y_{\min} - \hat{y}(\mathbf{x})}{\hat{s}\sqrt{2}}\right)\right] \qquad (32)$$

For a maximization problem, $I = \frac{Y(\mathbf{x}) - y_{\max}}{y_{\max}}$ (33)

2.2.4.3 Optimization using Expected Improvement

If the mean $\hat{y}(x)$ and the variance $\hat{s}^2(x)$ are provided, the amount of improvement over the current model can be determined. The Expected Improvement can be calculated by [30]:

$$E[I(x)] = \left(y_{min} - \hat{y}(x)\right)\Phi\left(\frac{y_{min} - \hat{y}(x)}{\hat{s}(x)}\right) + s\phi\left(\frac{y_{min} - \hat{y}(x)}{\hat{s}(x)}\right) \quad if\ s > 0 \qquad (34)$$

$$E[I(x)] = 0 \quad if\ s = 0 \qquad (35)$$

where $\Phi(.)$ and $\phi(.)$ are the cumulative distribution function and probability density function respectively. A maximum expected improvement infill procedure usually finds the global optimum. Using the error function, the expected improvement can be expressed as:

$$E[I(\mathbf{x})] = \left(y_{\min} - \hat{y}(\mathbf{x})\right)\left[\frac{1}{2} + \frac{1}{2}\mathrm{erf}\left(\frac{y_{\min} - \hat{y}(\mathbf{x})}{\hat{s}\sqrt{2}}\right)\right] + \hat{s}\frac{1}{\sqrt{2\pi}}\exp\left[\frac{-\left(y_{\min} - \hat{y}(\mathbf{x})\right)^2}{2\hat{s}^2}\right] \qquad (36)$$

In this work, the Efficient Global Optimization (EGO) algorithm [36] was used to find the best design possible. The flowchart for the simulation is shown in Figure 1. The Probability of Improvement and Expected Improvement were used as acquisition functions. After finding the initial best design, i.e., the maximum value of neck size from the simulation response values, the acquisition function is maximized using a genetic algorithm [37]. The optimal values of the design variables are determined and using those values, the new response is found out from the simulation model. This helps in updating the metamodel in each iteration. This process is continued till an adequately suitable design is obtained or until the maximum number of iterations i.e., 15 is reached. The following flowchart illustrates the workflow of the optimization routine.

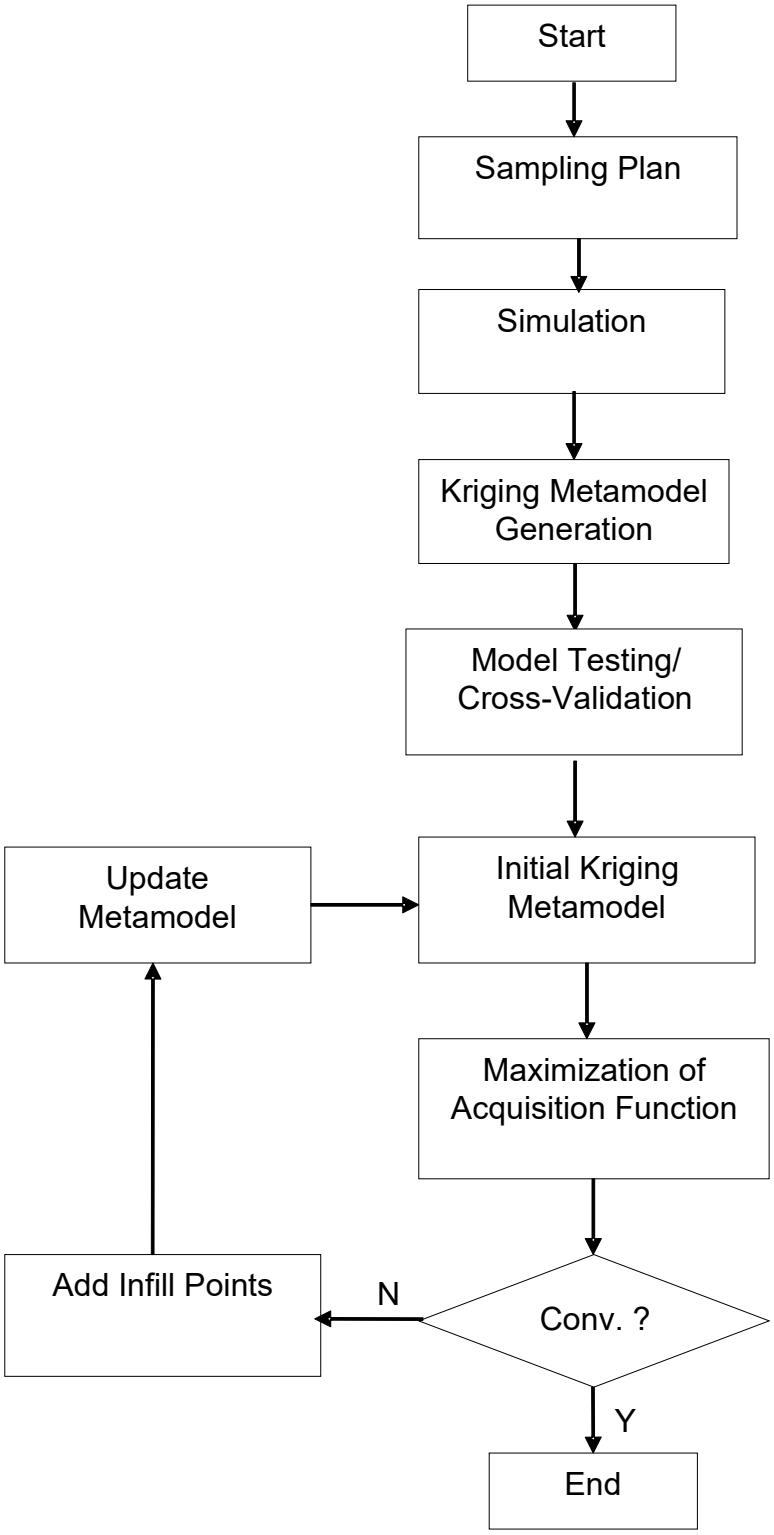

Figure 1: Flow chart of the Efficient Global Optimization algorithm used in this study

The optimization problem for equal-sized particles can be framed as:

$$\begin{aligned} &\text{Find} && \boldsymbol{x} \in \mathbb{R}^2 && (37)\\ &\text{Maximize} && N(x) \\ &\text{Subject to} && x_i \in \{4{,}40, \ldots, 24{,}41.5\} \end{aligned}$$

where $\boldsymbol{x} = \left(D_{surf}, d\right)$ is the vector of design variables surface diffusivity and inter-particle distance, and $N(\boldsymbol{x})$ is the neck size.

The Efficient Global Optimization (EGO) approach was used in this work for the following major advantages [36]: (1) Fewest function evaluations are required among other competing optimization methods. This is due to the possibility of interpolating or extrapolating accurately over large distances in the design space. (2) There is a credible stopping rule based on the acquisition function from further searching the surrogate. This is possible because the probabilistic model provides confidence intervals on the function's value at unsampled points, the validity of which can be checked by model validation techniques. (3) There is a fast approximation to the multi-physics simulation model that can be used to identify important variables and visualize the nature of input-output relationships.

3. Results and discussion

3.1 Sintered particle microstructure evolutions

Figure 2 depicts the microstructure evolution with the sizes of the two spherical particles being equal, using the phase-field code in Ref. [28]. In this case, it can be observed that the shrinkage of both particles takes place at an equal rate. The neck evolution is rapid at the beginning and

then slows down later. The changes in the size of the neck can be attributed to the transport of matter from regions in the vicinity with high concentration to the neck region facilitated by various diffusion paths.

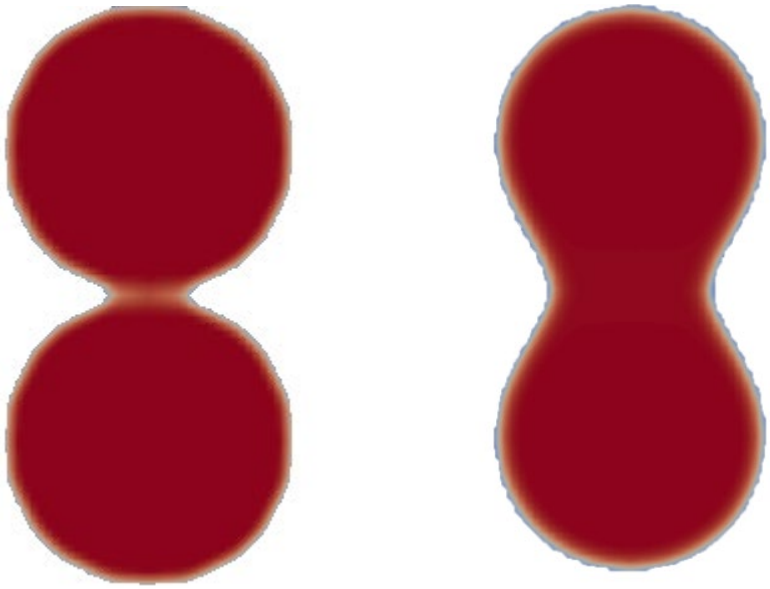

(a) (b)

Figure 2: Neck evolutions of the equalized particles (a) at time step 100, (b) at time step 20,000.

Figure 3 describes the evolution of the neck region for unequal-sized particles, i.e., particle size ratio of 1.5, using the phase-field code in Ref. [28]. It was observed that the neck formation was rapid in the early stages of the simulation but later slowed down and reached a steady state. It was also observed that the smaller particle had a faster contraction.

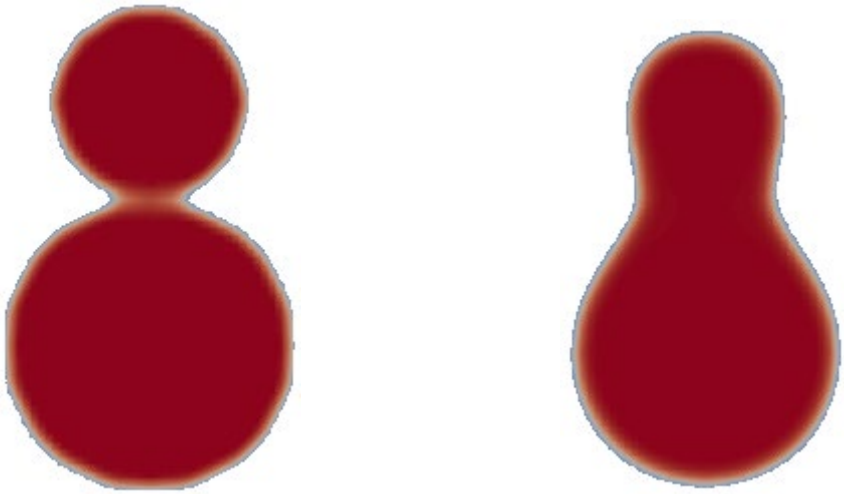

(a) (b)

Figure 3: Neck evolutions of the unequalized particles. (a) at time step 100, (b) at time step 20,000.

Figure 4 shows the evolution of the neck region sizes for both the equal and unequal sized particles models. The curves show the increase of neck size is steep at the beginning for both the particle sizes and then tends to flatten as the time step increases. In both cases, the surface diffusivity was fixed at 16. This indicates that the particle size does not have a significant effect on the evolution of neck size at later time steps.

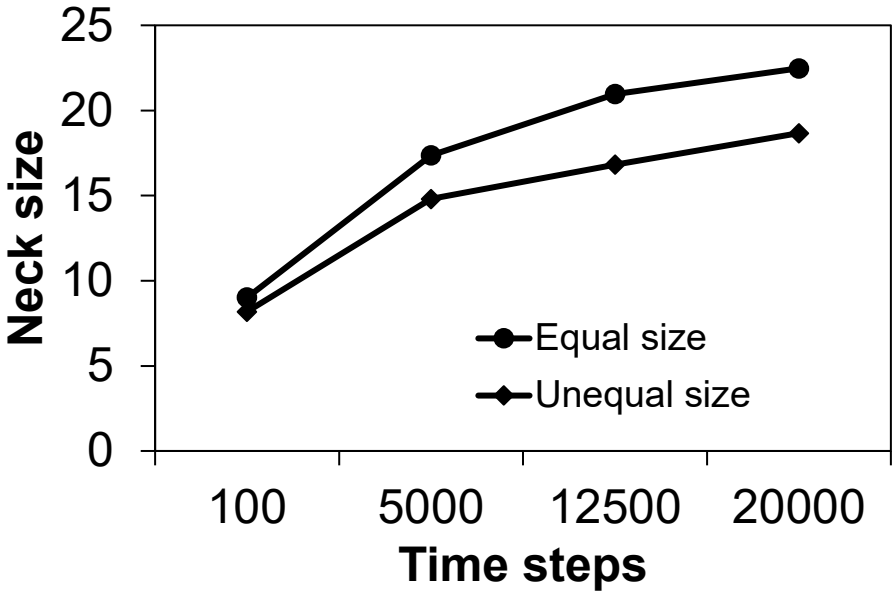

Figure 4: Evolution of neck size at different time steps for equal and unequal sized particles

3.2 Machine learning approach results

3.2.1 Equal sized particles

Figures 5,6, and 7 show the initial metamodels obtained using three regression functions Regpoly0, Regpoly1 and Regpoly2 which refer to polynomial approximations of orders zero, one and two, respectively. The standard practice is to use a constant regression function which is Regpoly0. This is done in order to avoid unwanted flexibility of the model which may lead to overfitting the noise in the data generated due to higher order polynomials. This eventually causes poor generalization capability of the model. The neck size is seen to increase with increasing surface diffusivity and decreases with increasing inter-particle distance.

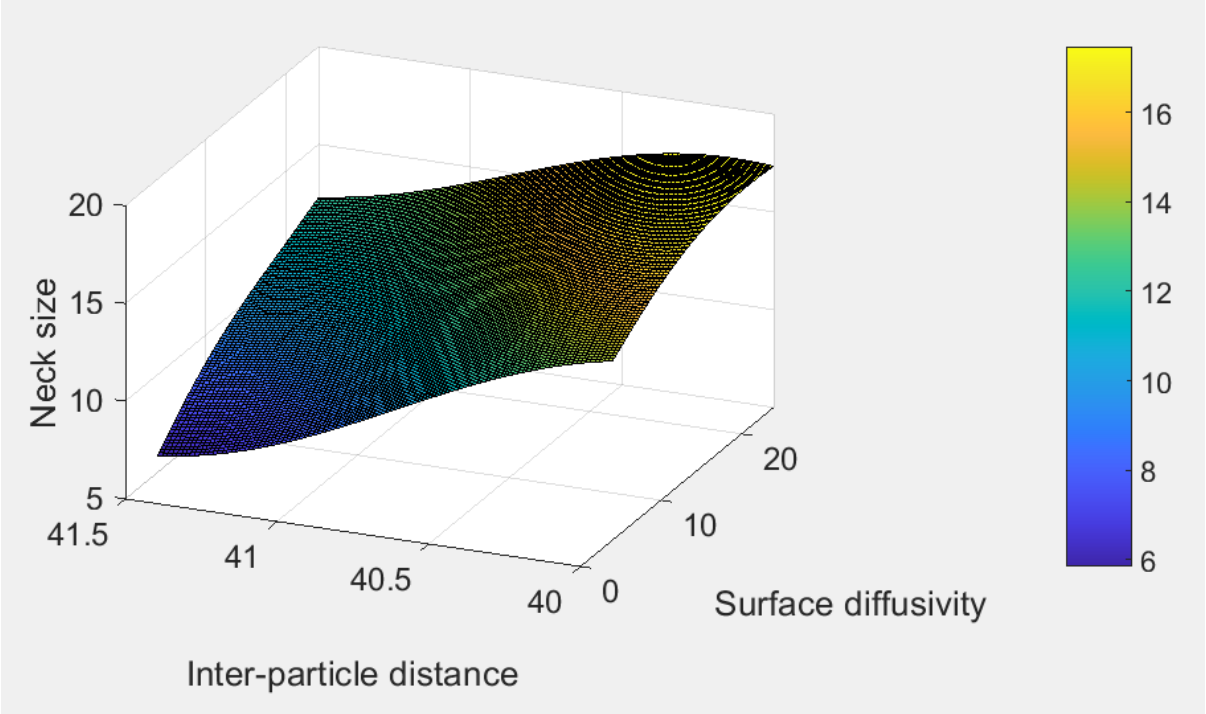

Figure 5: Metamodel by regression function of order zero for equal sized particle model

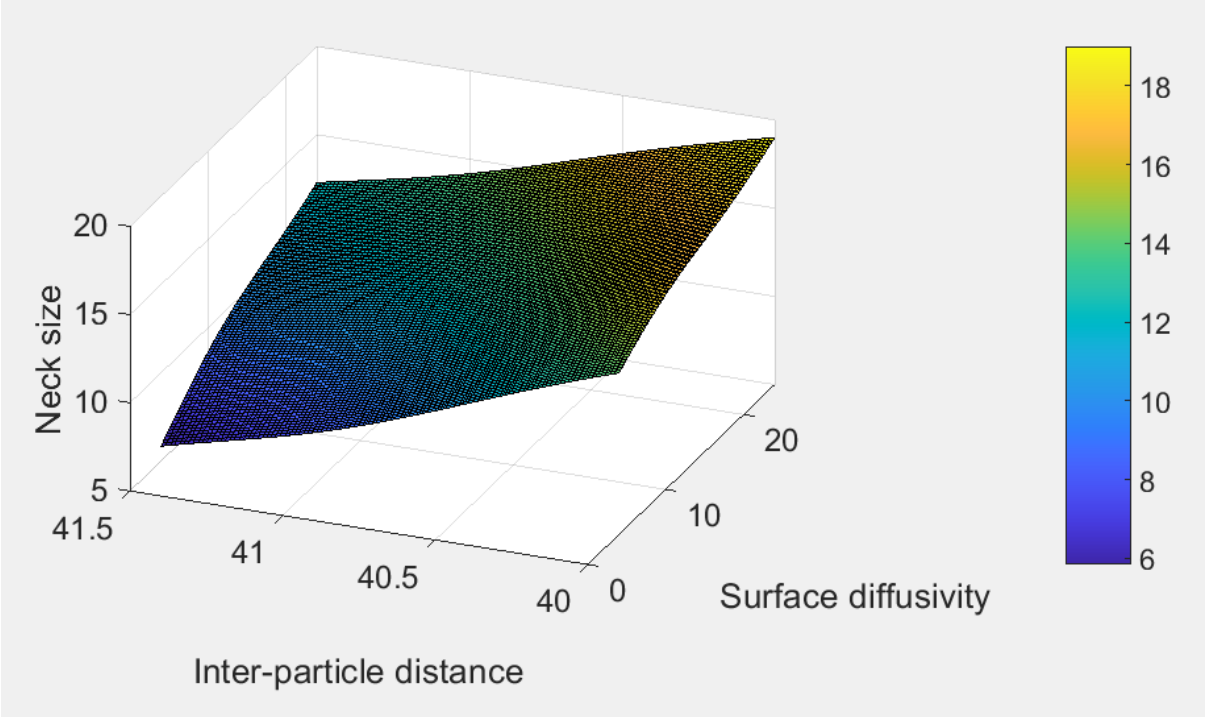

Figure 6: Metamodel by regression function of order one for equal sized particle model

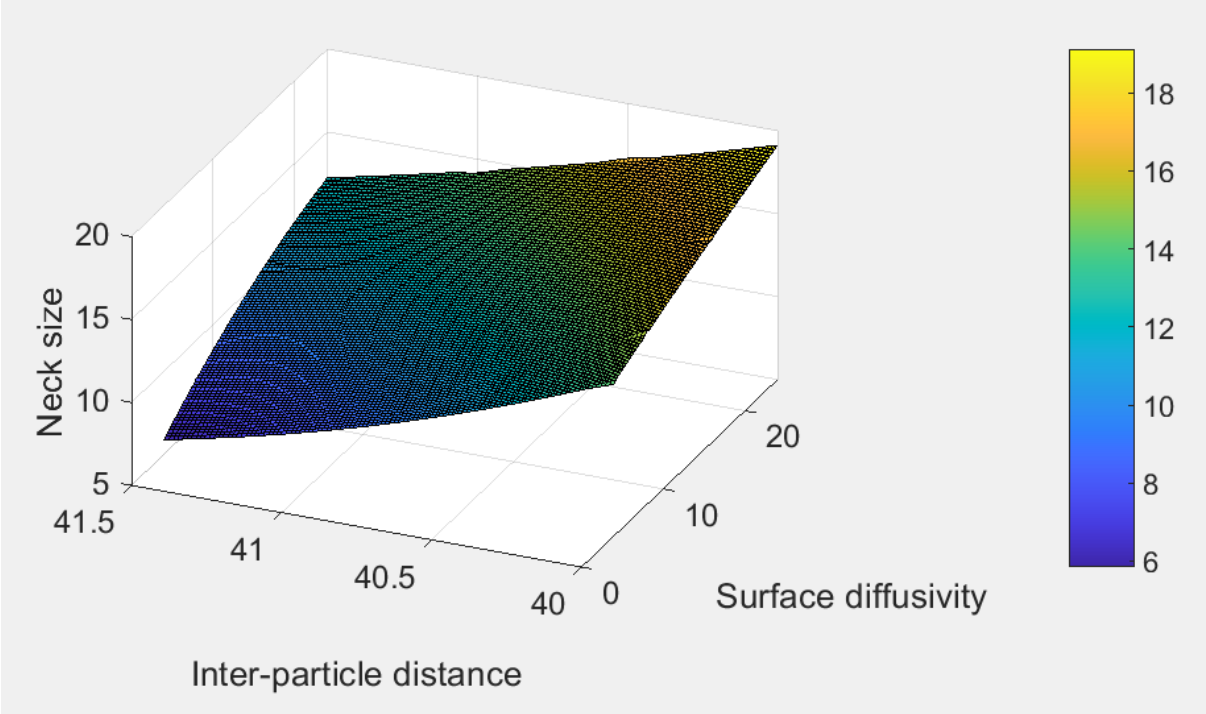

Figure 7: Metamodel by regression function of order two for equal sized particle model

For model testing, the root mean square error (RMSE) values for each initial metamodel were calculated as 1.2077, 1.2205, and 1.3937 for Regpoly0, Regpoly1, and Regpoly2, respectively. The model with the regression function of order zero was found to have the least RMSE of 1.2077 and hence was selected for the further optimization process.

For cross-validation, the average error found by cross-validation for the observations used to build the surrogate model is 0.25836, 0.38635, and 0.32083 for Regpoly0, Regpoly1, and Regpoly2, respectively. Again, the model with the regression function of order zero has the least error of 0.25836. Hence error results from both model testing and cross-validation indicate Regpoly0 is the best metamodel for equal-sized particles.

Figure 8 presents the correlation of surface diffusivity and inter-particle distance with neck size, which shows a strong correlation with a correlation coefficient of 0.5733. This is because as the surface diffusivity increases, there is a large increase in neck size.

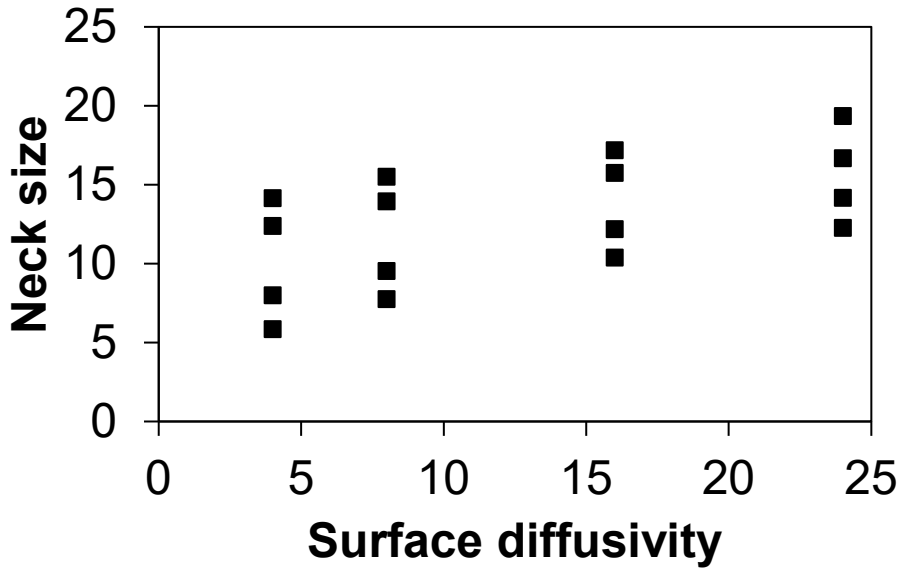

Figure 8: Correlation between surface diffusivity and neck size for equal sized particle model

Figure 9 explains that the inter-particle distance is strongly associated with the neck size with a Pearson correlation coefficient of -0.8028. As the inter-particle distance increases, there is a large decrease in neck size.

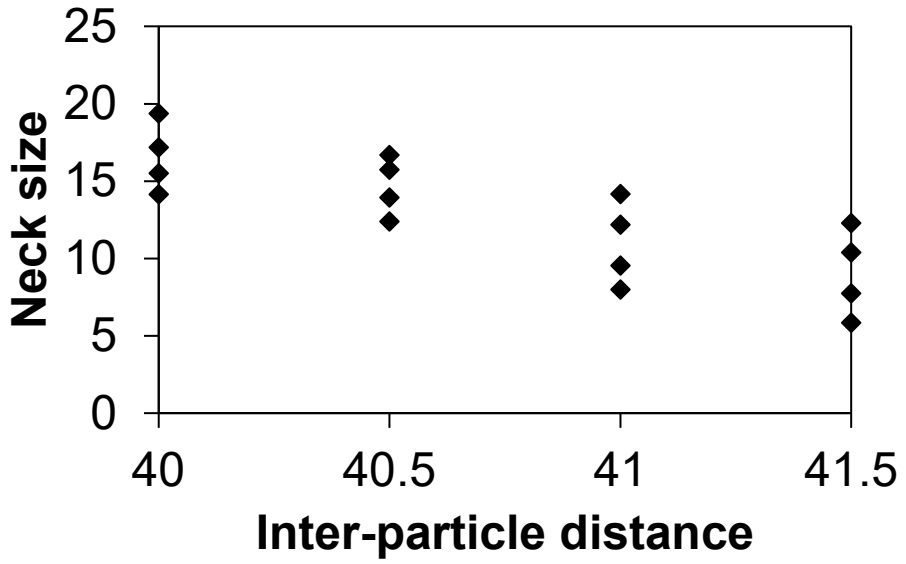

Figure 9: Correlation between inter-particle distance and neck size for equal sized particle model

For optimization by Probability of Improvement (PI) as the acquisition function, the random sampling plan was used with a surface diffusivity range from 4 to 24 and inter-particle distance from 40 to 41.5. Using the metamodel generated by Gaussian Process Regression, the results show a monotonic nature of the data for neck size linearly increasing with increasing surface diffusivity and decreasing with inter-particle distance. At the last iteration in the optimization process, the values of optimal design variables converged at [23.8268, 40.0001]. Hence the iteration was stopped here. The maximum neck size was 19.0476 and the Probability of Improvement 0.5119.

Additionally, using Expected Improvement (EI) as the acquisition function, the initial metamodel generated by Kriging regression and its re-iterations show that the neck size linearly increases with increasing surface diffusivity and decreases with increasing inter-particle distance. After 15 iterations in the optimization process, the values of optimal design variables

were found as [23.9874, 40.7428]. The maximum neck size was 19.0476 and the Expected Improvement 8.1805×10^{3}. The solution obtained looks like a global optimum as all potential values seem to have been explored from the entire design space.

3.2.2 Unequal sized particles

A. Initial Metamodel Generation

For unequal-sized particles, Figures 10, 11, and 12 show the initial metamodels obtained using three regression models with polynomials of order zero (Regpoly0), one (Regpoly1), and two (Regpoly2) respectively. The figures have the surfaces that detail the monotonic increase of neck size with an increase in surface diffusivity and decreasing neck size with an increase in inter-particle distance. The neck size increased from 12.093 to 14.68752 for an inter-particle distance of 33.3, from 6.82169 to 12.06348 for an inter-particle distance of 34.3, and from 4.30771 to 10.39367 for an inter-particle distance of 34.8. The surface diffusivity ranged from 4 to 24 and inter-particle distance spanned 33.3 through 34.8.

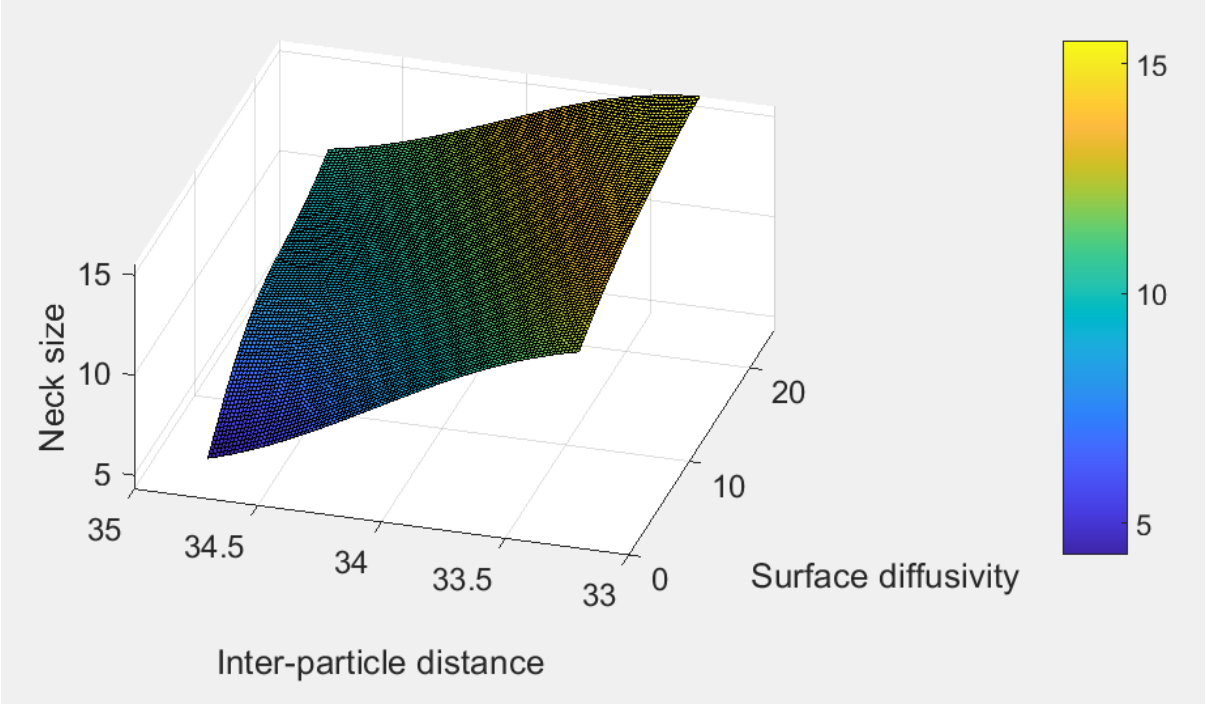

Figure 10: Metamodel by regression function of order zero for unequal sized particle model

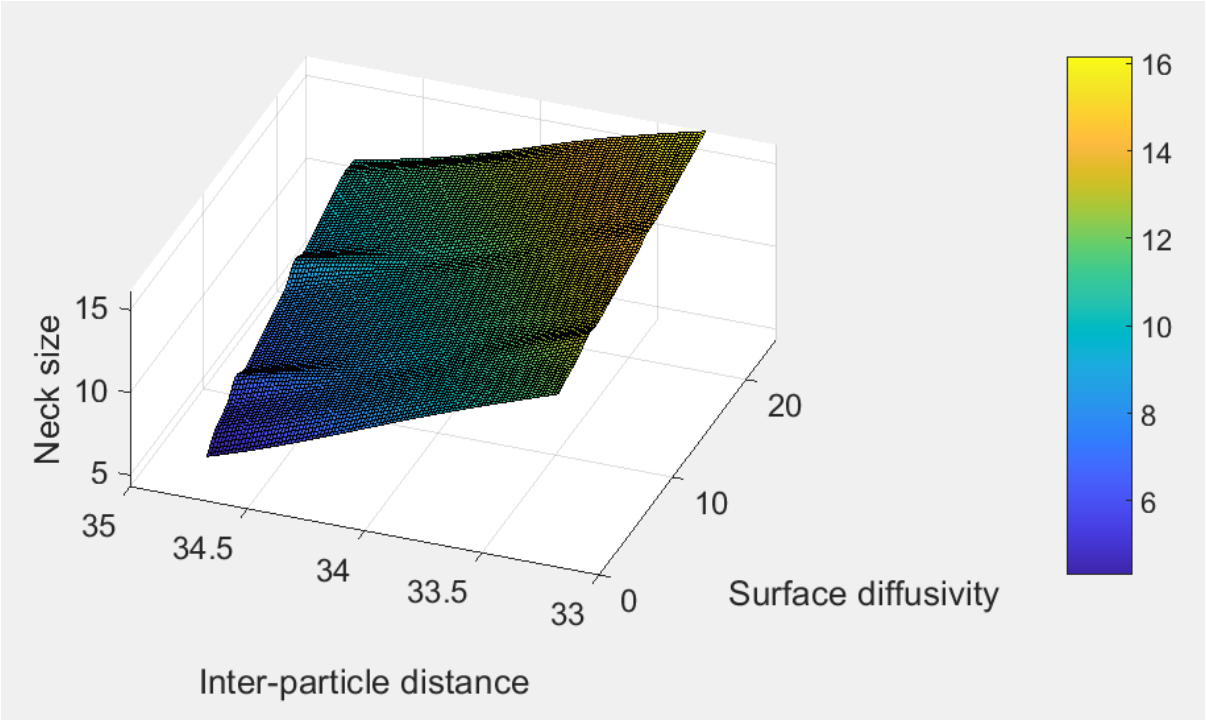

Figure 11: Metamodel by regression function of order one for unequal sized particle model

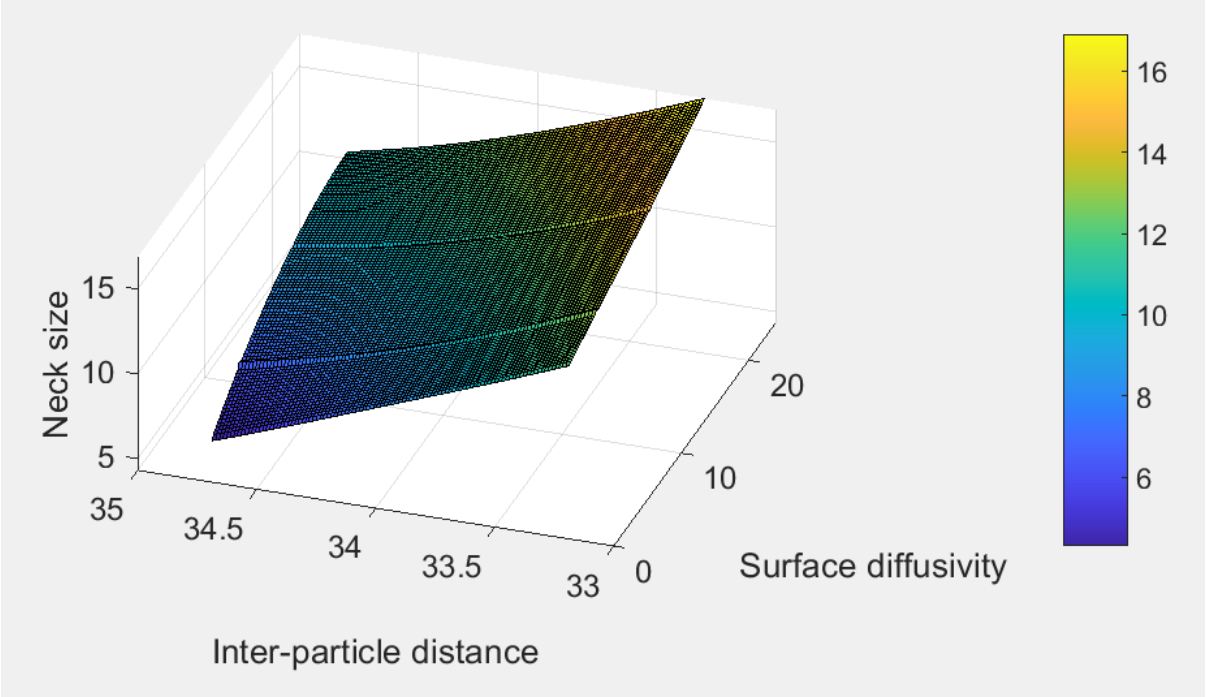

Figure 12: Metamodel by regression function of order two for unequal sized particle model

For model testing, the RMSE values for each metamodel are 0.4111, 0.7734, and 1.0878 for Regpoly0, Regpoly1, and Regpoly2, respectively. Since order zero was found to have the least RMSE of 0.4111, hence it was chosen for Bayesian optimization. For both equal and unequal-sized particles, the model with the regression function of order zero gave the least mean square error. Also, the error was observed to decrease in unequal-sized particles.

The average error found by leave-one-out cross-validation for the observations was used to build the surrogate model of unequal-sized particles. The cross-validation errors at different regression functions for unequal sized particles are 0.3149, 0.5850, and 0.4362 for Regpoly0, Regpoly1, and Regpoly2, respectively. The model with the regression function of order zero has the least error of 0.3149. The error results from model testing and cross-validation for unequal-sized particles indicate Regpoly0 is the suitable metamodel to start the optimization process with. This result concurs with that of equal-sized particles. The cross-validation error is greater for unequal-sized particles than equal-sized particles.

For sensitivity analysis, the correlations of surface diffusivity and inter-particle distance with neck size respectively were calculated. There is a strong positive correlation between surface diffusivity and neck size with a coefficient of 0.5734, and there is a strong dependence of neck size on inter-particle distance with a Pearson correlation coefficient of -0.7960. As the inter-particle distance increases, there is a considerable decrease in neck size. This proves that the nature of the correlation between the QOI and input parameters is independent of the particle size.

For optimization using Probability of Improvement, the random sampling plan was used with surface diffusivity ranging from 4 to 24 and inter-particle distance from 33.3 to 34.8. The first metamodel generated by Gaussian Process Regression with neck size linearly increases for the range of surface diffusivity and decreasing for that of inter-particle distance.

The values of optimal design variables were fixed at [23.9700, 33.3005] after exhausting all 15 iterations in the optimization process. The maximum neck size was 16.1905 and the Probability of Improvement was 0.4999.

Additionally, for optimization using Expected Improvement, the input sampling plan was used with surface diffusivity ranging from 4 to 24 and inter-particle distance from 33.3 to 34.8. The results show that the initial metamodel generated by Kriging regression and the increasing nature of the neck size with increasing surface diffusivity and decreasing with inter-particle distance.

At the end of 15 iterations, the values of design variables converged at [23.9893, 33.9627], the maximum neck size being 16.1905 and Expected Improvement as 6.0914×10^{3}. The solution obtained here tends to be a global optimum.

For the Probability of Improvement at each iteration for unequal-sized particles, initially, the PI decreases and tends to zero, then becomes constant in the later iterations. The trend is similar to the case for equal-sized particles but here the function will apparently require more than 15 iterations to eventually turn zero.

The final optimal values of design variables surface diffusivity D_{surf} and inter-particle distance d as obtained from the two acquisition functions: For equal-sized particles, the Probability of Improvement gives the optimal result as [23.8268, 40.0001] when the design converged after 10 iterations. The Expected Improvement after 15 iterations provides an optimal design of

[23.9874, 40.7428] which indicates a global optimum. For unequal-sized particles, the Probability of Improvement provides a solution of [23.9700, 33.3005] while the Expected Improvement provides optimal values of [23.9893, 33.9627] after consuming all 15 iterations.

The maximum value of surface diffusivity present in the sampling plan is 24. The minimum values of inter-particle distance in the sampling plans are 40 and 33.3 for equal-sized and unequal-sized particles respectively. Hence, the optimization result validates the theory that surface diffusivity should be as high as possible to have better densification of the material undergoing sintering. The optimal values of inter-particle distance emphasize the fact that lower inter-particle distance leads to a close-packed arrangement of atoms and hence reduction of porosity between the particles. This leads to better mechanical properties of the material.

4. Conclusions and future work

In the current work, a machine-learning framework has been developed to aid in quality control of the sintering process in additively manufactured materials. Specifically, the two-particle microstructure evolution during the process was optimized. The following conclusions can be drawn:

1. With increasing surface diffusivity, the neck size between particles always increases irrespective of the particle radii. For equal-sized particles, the neck size increased from 14.15388 to 19.36508 with an increase of surface diffusivity from 4 to 24 and inter-particle distance constant at 40. For unequal-sized particles, the neck size increased from 12.093 to 15.55554 with the same increase of surface diffusivity and inter-particle distance constant at 33.3. This is because surface diffusivity increases densification in the material and hence enlargement of neck width occurs.

2. The neck size decreases with an increase in inter-particle distance independent of particle radii. For equal-sized particles, the neck size decreased from 14.15388 to 5.84617 with an increase of inter-particle distance from 40 to 41.5 at constant surface diffusivity of 4. For unequal-sized particles, the neck size decreased from 12.093 to 4.30771 for an increase of inter-particle distance from 33.3 to 34.8 with a constant surface diffusivity of 4. This is attributable to the fact that lesser inter-particle distance leads to a reduction in porosity and hence better densification due to a close-packed arrangement of particle microstructure. This helps in enhancing material properties.
3. The sensitivity analysis shows that inter-particle distance has a higher contribution to the variation of neck size than that of surface diffusivity irrespective of particle size. For equal-sized particles, the value of the correlation coefficient between surface diffusivity and neck size is 0.5733 which indicates a strong positive correlation. The same conclusion can be drawn from the value for unequal-sized particles which are 0.5734. The correlation coefficients between inter-particle distance and neck size for equal and unequal sized particles are -0.8028 and -0.7960 respectively which indicate a strong negative association of inter-particle distance with neck size. As the values are closer to -1, the lesser the inter-particle distance, the more the value of neck size should be. Hence, to get better mechanical properties of the material, it is recommended to have the inter-particle distance as small as possible and surface diffusivity as high as possible.
4. For both equal-sized and unequal-sized particles, the metamodel with the regression function of order zero (Regpoly0) is the best initial metamodel. The root mean square error and cross-validation error for Regpoly0 for equal-sized particles are 1.2077 and 0.25836. The same for unequal sized particles are 0.4111 and 0.3149.

5. The optimization result from two different acquisition functions looks in good agreement with each other. For equal-sized particles, the Probability of Improvement offers the optimal values of design variables, surface diffusivity, and inter-particle distance as 23.8268 and 40.0001, while Expected Improvement provides the values 23.9874 and 40.7428 respectively. For unequal-sized particles, the optimal design values from Probability of Improvement were 23.9700 and 33.3005 while those from Expected Improvement were 23.9893 and 33.9627.

Although the insightful optimization results achieved in this work, there are still a few limitations that can be included in the future work. A powder bed, including the one in the AM processes, can be modeled with randomly packed particles with a particle size distribution, e.g., [38]. The current work is intended to provide a base line data using a two-particle model, and the focus is on understanding the optimization process. In the future, a more realistic packed powder bed can be included.

Acknowledgments

A fruitful discussion with Prof. Xiaoping Du regarding uncertainty quantification is highly appreciated. Sugrim Sagar is supported by the IUPUI University Diversity Fellowship and the Indiana University Diversity Dissertation Fellowship, and Xuehui Yang is supported by the Research Foundation doctoral thesis research award by Indiana University – Purdue University Indianapolis.

References

1. Zhang, Y., Y.-G. Jung, and J. Zhang, *Multiscale Modeling of Additively Manufactured Metals: Application to Laser Powder Bed Fusion Process*. 2020: Elsevier.
2. Wikipedia. *Selective laser sintering (https://en.wikipedia.org/wiki/Selective_laser_sintering, accessed January 2021)*. 2021.
3. Wang, Y.U., *Computer modeling and simulation of solid-state sintering: A phase field approach.* Acta Materialia, 2006. **54**(4): p. 953-961.
4. Demirskyi, D., et al., *Peculiarities of the neck growth process during initial stage of spark-plasma, microwave and conventional sintering of WC spheres.* Journal of Alloys and Compounds, 2012. **523**: p. 1-10.
5. Xu, X., P. Lu, and R.M. German, *Densification and strength evolution in solid-state sintering Part II Strength model.* Journal of Materials Science, 2002. **37**(1): p. 117-126.
6. German, R.M., *Sintering Theory and Practice*. 1996: Wiley-Interscience.
7. German, R.M., *Strength evolution in debinding and sintering*, in *Proceedings of Sintering 2003 the 3rd International Conference on the Science, Technology & Applications of Sintering*. 2003: University Park, PA.
8. Pavan, M., et al., *CT-based quality control of Laser Sintering of Polymers.* Case studies in nondestructive testing and evaluation, 2016. **6**: p. 62-68.
9. Dotchev, K. and W. Yusoff, *Recycling of polyamide 12 based powders in the laser sintering process.* Rapid Prototyping Journal, 2009.
10. Karapatis, N., et al. *Optimization of powder layer density in selective laser sintering*. in *1999 International Solid Freeform Fabrication Symposium*. 1999.
11. Zarringhalam, H., C. Majewski, and N. Hopkinson, *Degree of particle melt in Nylon-12 selective laser-sintered parts.* Rapid Prototyping Journal, 2009.
12. Phillips, T., S. Fish, and J. Beaman, *Development of an automated laser control system for improving temperature uniformity and controlling component strength in selective laser sintering.* Additive Manufacturing, 2018. **24**: p. 316-322.
13. Wegner, A. and G. Witt. *Process monitoring in laser sintering using thermal imaging*. in *SFF Symposium, Austin, Texas, USA*. 2011.
14. Olakanmi, E.O., *Effect of mixing time on the bed density, and microstructure of selective laser sintered (sls) aluminium powders.* Materials Research, 2012. **15**(2): p. 167-176.
15. Olakanmi, E., R. Cochrane, and K. Dalgarno, *Densification mechanism and microstructural evolution in selective laser sintering of Al–12Si powders.* Journal of Materials Processing Technology, 2011. **211**(1): p. 113-121.
16. Biswas, S., et al., *A study of the evolution of microstructure and consolidation kinetics during sintering using a phase field modeling based approach.* Extreme Mechanics Letters, 2016. **7**: p. 78-89.
17. Hötzer, J., et al., *Phase-field simulation of solid state sintering.* Acta Materialia, 2019. **164**: p. 184-195.
18. Biswas, S., D. Schwen, and V. Tomar, *Implementation of a phase field model for simulating evolution of two powder particles representing microstructural changes during sintering.* Journal of materials science, 2018. **53**(8): p. 5799-5825.
19. Asp, K. and J. Ågren, *Phase-field simulation of sintering and related phenomena–A vacancy diffusion approach.* Acta materialia, 2006. **54**(5): p. 1241-1248.
20. Kumar, V., Z. Fang, and P. Fife, *Phase field simulations of grain growth during sintering of two unequal-sized particles.* Materials Science and Engineering: A, 2010. **528**(1): p. 254-259.

21. Dzepina, B., D. Balint, and D. Dini, *A phase field model of pressure-assisted sintering.* Journal of the European Ceramic Society, 2019. **39**(2-3): p. 173-182.
22. Termuhlen, R., et al., *Three-dimensional phase field sintering simulations accounting for the rigid-body motion of individual grains.* Computational Materials Science, 2020. **186**: p. 109963.
23. Swaroop, A., V. Himasree, and T. Thomas, *Machine learning based a priori prediction on powder samples of sintering-driven abnormal grain growth.* Computational Materials Science. **187**: p. 110117.
24. Song, L., et al., *Synthetically predicting the quality index of sinter using machine learning model.* Ironmaking and Steelmaking, 2019: p. 1-9.
25. Xiao, L., M. Lu, and H. Huang, *Detection of powder bed defects in selective laser sintering using convolutional neural network.* The International Journal of Advanced Manufacturing Technology, 2020. **107**(5): p. 2485-2496.
26. Wu, Z., et al., *Transfer learning aid the prediction of sintering densification.* Ceramics International, 2020. **46**(16): p. 25200-25210.
27. Zhang, J.-h., A.-g. Xie, and F.-m. Shen, *Multi-objective optimization and analysis model of sintering process based on BP neural network.* Journal of Iron and Steel Research, International, 2007. **14**(2): p. 1-5.
28. Biner, S.B., *Programming phase-field modeling*. 2017: Springer.
29. Rasmussen, C.E. *Gaussian processes in machine learning*. in *Summer School on Machine Learning*. 2003. Springer.
30. Forrester, A., A. Sobester, and A. Keane, *Engineering design via surrogate modelling: a practical guide*. 2008: John Wiley & Sons.
31. Anderson, M.J. and P.J. Whitcomb, *Design of experiments.* Kirk-Othmer Encyclopedia of Chemical Technology, 2000: p. 1-22.
32. Couckuyt, I., T. Dhaene, and P. Demeester, *ooDACE toolbox: a flexible object-oriented Kriging implementation.* Journal of Machine Learning Research, 2014. **15**: p. 3183-3186.
33. Friedman, J., T. Hastie, and R. Tibshirani, *The elements of statistical learning*. Vol. 1. 2001: Springer series in statistics New York.
34. Saltelli, A., et al., *Global sensitivity analysis: the primer*. 2008: John Wiley & Sons.
35. Ghosh, S., et al., *Uncertainty analysis of microsegregation during laser powder bed fusion.* Modelling and Simulation in Materials Science and Engineering, 2019. **27**(3): p. 034002.
36. Jones, D.R., M. Schonlau, and W.J. Welch, *Efficient global optimization of expensive black-box functions.* Journal of Global optimization, 1998. **13**(4): p. 455-492.
37. Whitley, D., *A genetic algorithm tutorial.* Statistics and Computing, 1994. **4**(2): p. 65-85.
38. Yang, Y., et al., *3D non-isothermal phase-field simulation of microstructure evolution during selective laser sintering.* npj Computational Materials, 2019. **5**(1): p. 81.